Sensors & Actuators: B. Chemical 386 (2023) 133731

Contents lists available at ScienceDirect

Sensors and Actuators: B. Chemical

journal homepage: www.elsevier.com/locate/snb

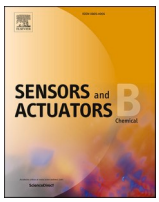

Dye disaggregation light-up aptamer for super-resolution RNA imaging

Chunyu Yan [a,b], Lu Miao [b,*], Yan Zhang [a,b], Xuelian Zhou [a,b], Guangying Wang [a,b], Yueqing Li [c,*], Qinglong Qiao [b,*], Zhaochao Xu [a,b,**]

[a] Zhang Dayu School of Chemistry, Dalian University of Technology, 2 Linggong Road, Dalian 116024, China
[b] CAS Key Laboratory of Separation Science for Analytical Chemistry, Dalian Institute of Chemical Physics, Chinese Academy of Sciences, 457 Zhongshan Road, Dalian 116023, China
[c] State Key Laboratory of Fine Chemicals, Department of Pharmaceutical Sciences, School of Chemical Engineering, Dalian University of Technology, 2 Linggong Road, Dalian 116012, China

ARTICLE INFO

Keywords:
RNA imaging
Aptamer
Fluorophore
Dye aggregate
Super-resolution imaging

ABSTRACT

Genetically encoded light-up RNA aptamers have become powerful tools for visualizing RNAs in cells. However, fluorogenic dye/aptamer pairs used for super-resolution RNA imaging are still rare. Herein, we reported an environment-sensitive dye **Nap** which can light up its target RNA aptamer **NapRA** for aptamer-based RNA imaging with confocal and structured illumination microscopy (SIM). **Nap** was designed to be amphiphilic to assemble into nano-particles in water associated with the quenched fluorescence by the aggregation effects. **NapRA** was obtained from SELEX technology with a 12-round **Nap**-based selection and has a high binding affinity to **Nap** of K_d = 3.142 nM. The super affinity disintegrated the dye aggregate and resulted in a turn-on fluorescent signal. The light-up feature combined with high photostability made **Nap**/**NapRA** a useful system capable of super-resolution imaging of the expression of RNA in bacteria. This work represents the first application of dye aggregation-disaggregation for aptamer-based RNA imaging.

1. Introduction

Applicable RNA labeling methods combined with advanced fluorescence imaging techniques (e.g., super-resolution imaging) enable dynamic imaging of RNA in cells with high temporal and spatial resolution, providing insight into the complex biological processes of RNA [1]. The performance and labeling characteristics of fluorescent probes are important factors in achieving final high-quality images, especially for super-resolution RNA imaging [2,3]. Fluorescence in situ hybridization (FISH) and molecule beacons were the earliest RNA labeling methods, but their application was limited by non-permeability, instability, and uneven cellular distribution of the fluorophore-nucleic acid complexes [4–6]. Subsequently, the interaction between RNA-binding protein (RBP) and aptamer was used to label the RNA of a target. Usually, tens of repeated RBP-binding aptamers were incorporated into the 3′-untranslated region of the target messenger RNA (mRNA). And then fluorescent proteins fused RBPs (FPs-RBP) were genetically encoded in the same cell allowing for tracking mRNA [7–11]. This method has been considered a gold reference for collecting data on gene expression and RNA trafficking. However, high background fluorescence and dozens of bulky protein tags may affect the movement and function of RNA. And the easy photo-bleaching of fluorescent proteins limits the long-term super-resolution imaging of mRNA [12]. Recently, fluorogenic dye/aptamer pairs have been considered a promising RNA imaging tool, where the large FPs-RBP complexes were replaced by a dye with cellular permeability and spectral flexibility [13,14]. These small molecule probes with high specificity and affinity are non-fluorescent in solution, but the fluorescence would be turned on when the dye specifically recognizes the target RNA aptamer [15–18].

A variety of fluorogenic dye-aptamer pairs have already been identified in vitro using the systematic evolution of ligands by exponential enrichment (SELEX) technology [19,20]. Among them, three strategies were used to light up the fluorescence of dyes. The most used one is to restrict the vibrational and rotational motion of the fluorophore, such as Malachite green (MG) [21], GFP fluorophore-like synthetic dye DFHBI [13,17], DFHO [15,18] and HBC [22]. As the first dye turned on by RNA normally, MG has extremely low quantum yields due to easy vibrational de-excitation, but RNA aptamer could enhance the fluorescence by

* Corresponding authors.
** Corresponding author at: Zhang Dayu School of Chemistry, Dalian University of Technology, 2 Linggong Road, Dalian 116024, China.
E-mail addresses: miaolu@dicp.ac.cn (L. Miao), yueqingli@dlut.edu.cn (Y. Li), qqlqiao@dicp.ac.cn (Q. Qiao), zcxu@dicp.ac.cn (Z. Xu).

https://doi.org/10.1016/j.snb.2023.133731
Received 4 March 2023; Received in revised form 22 March 2023; Accepted 23 March 2023
Available online 25 March 2023

restricting such vibrations [21]. Another strategy is the inhibition of the fluorescence quenching pathway by electron transfer or energy transfer, such as Förster resonance energy transfer (FRET) [23], photoinduced electron transfer (PET) [24–26] and intramolecular fluorophore π-π stacking [16,27]. For instance, Gemini-561 was non-emissive in water because of intramolecular dimerization-induced self-quenching of sulforhodamine B fluorophores, and its RNA aptamer o-Coral was capable of selectively separating the dimer and thus activating its fluorescence [16]. The third strategy is based on the fluorescence light and dark changes caused by the equilibrium of the rhodamine spironolactone switch. For example, Si-rhodamine exists in the solution as a non-fluorescent spironolactone structure. After specific binding to RNA aptamer SiRA, the fluorescence of Si-rhodamine was subsequently lighted up by the formation of a zwitterion state [28]. For aptamer selective fluorogenic probes, dye brightness, photostability, biocompatibility, and signal-to-noise ratio are critical for image quality. Only TMR-DN and SiRs dyes reported by Jaschke's et al. were currently available for RNA super-resolution imaging [28,29]. Indeed, dyes with positive charges like rhodamine tend to bind mitochondria to produce high-intensity background signals. Therefore, fluorogenic aptamer probes capable of super-resolution imaging of RNA are still required.

In this work, the probe **Nap** was reported to light up target RNA aptamer for aptamer-based RNA imaging with confocal microscopy and structured illumination microscopy (SIM). **Nap** was derived from naphthalimide fluorophore, which was a traditional environment-sensitive fluorophore. As shown in Scheme 1, the neutral naphthalimide fluorophore acted as a hydrophobic group, while the amino and amide groups were hydrophilic, allowing **Nap** self-assemble into fluorescence quenched nano-particles. After the addition of RNA aptamer **NapRA** which has a nanomolar level affinity for **Nap**, this strong binding induced the disassembly of the **Nap**-based nanoparticles, resulting in a turn-on and relatively stable fluorescent signal. The aggregation-disaggregation of **Nap** was confirmed by dynamic light scattering (DLS), fluorescence, and SEM imaging. Molecular docking simulation was further used to investigate the binding mechanism between **Nap** and **NapRA**. Finally, this aptamer/fluorophore recognition induced light-up system was used as a gene coding tag to visualize mRNA in bacteria.

2. Experiment and methods

2.1. Materials

The oligonucleotide was chemically synthesized by General Biosystems Co., Ltd. Taq Plus DNA Polymerase, dNTP 10 mM Mixture, dN(U)TP 25 mM Mixture, T7 RNA Polymerase, Urea, Acrylamide, Acryl/Bis 30 % Solution (29:1), Water-DEPC Treated Water, RNase-free double-distilled water (ddH_2O), DNase I, RNase Inhibitor, Glycogen, Ethidium bromide, and NHS-Activated Sefinose (TM) 4 Fast Flow were obtained from Sangon Biotech. Restriction enzyme Prime Script™ 1st Strand cDNA Synthesis Kit was purchased from Takara. Trans5α and BL21(DE3) Chemically Competent Cell were bought from Trans Gen Biotech. Phenol was purchased from Solarbio. Hieff Clone® Plus Multi One Step Cloning Kit, MolPure® PCR Purification Kit, MolPure® Gel Extraction Kit, and MolPure® Plasmid Mini Kit were bought from Yeasen. Unless otherwise specifically stated, all reagents were used without further treatment or purification. The plasmids used in this paper were purchased from Addgene and Ningbo bionice biotechnology, respectively.

2.2. Spectra and particle size determination

The stock solution (2 mM) of **Nap** was prepared in DMSO. To investigate the solvation effect, 1 μM **Nap** was dissolved in different solvents including Toluene, Chloroform ($CHCl_3$), Ethyl acetate (EA), Dioxane, Acetone, Ethyl alcohol (EtOH), Acetonitrile (ACN), Dimethyl sulfoxide (DMSO) and water. The fluorescence spectra were detected with 450 nm light excitation. To measure the aggregation-disaggregation properties of **Nap**, aqueous solutions of 1 μM **Nap** were treated with 0–50 mM four types of surfactants including Dodecyltrimethyl ammonium chloride (DTAC, cationic surfactants), Sodium dodecyl sulfonate (SDS, anionic surfactant), T-octylphenoxypolyethoxyethanol (Triton X-100, nonionic surfactant) and Dodecyl dimethyl betaine (BS-12, zwitterionic surfactant). As the pH changes from pH 2–7 in aqueous solutions containing surfactant Triton X-100, the fluorescence spectra of **Nap** were examined.

To determine the size of **Nap** aggregates, 5 μM **Nap** was determined by Zetasizer nanosize analyzer in an aqueous solution with and without 50 μM NapRA. To monitor the changes in **Nap** aggregates, the solution

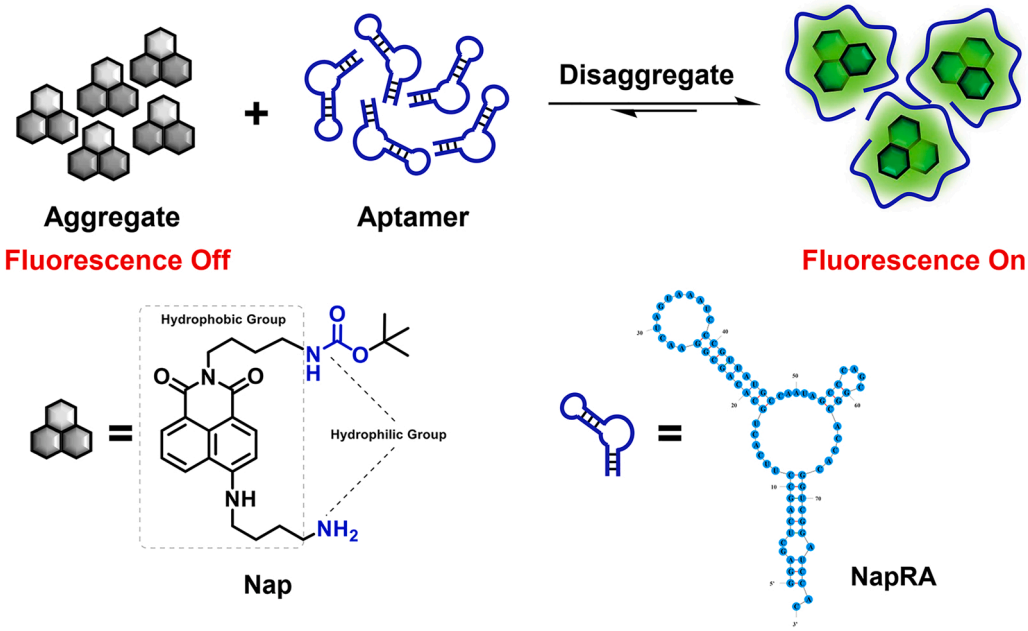

Scheme 1. Schematic illustration of fluorogenic RNA labeling strategy based on aggregation-disaggregation of **Nap**.

of 5 μL **Nap** and the complex solution of 5 μL **Nap/NapRA** were dripped onto a silicon wafer, respectively. And the dried samples were observed at 3 kV LED with a JSM-7800F scanning electron microscopy (SEM). To take confocal images, we dropped 5 μL **Nap** and 5 μL **Nap/NapRA** complex solution on a confocal imaging dish and covered them with a thin layer of agarose gel, respectively. The images were collected using a 100 × oil lens on an Olympus laser scanning confocal microscope (FV1000) under the conditions of $\lambda_{ex} = 488$ nm, $\lambda_{em} = 500–550$ nm.

2.3. Aptamer selection by systematic evolution of ligands by exponential enrichment (SELEX) technology

2.3.1. Library preparation

The random library was a variant derived from the library used commonly in Dye-based SELEX [22,28]. In brief, a 79-nt single-stranded oligonucleotide was synthesized to prepare the ssDNA library. It contains a 40-nt random region (Table S1 red) between 20-nt and 19-nt two constant fixed primer binding sites. The oligonucleotide was synthesized with an A:C:G:T ratio of 3:3:2:2. Following, we synthesized 38-nt and 20-nt primers which included a T7 promoter recognition site for RNA transcription in vitro. The oligonucleotide was purified by PAGE and 1 OD of the oligonucleotides were amplified in a 10 mL PCR reaction for 8-cycles (95 °C 5 min; cycles of 95 °C 30 s, 52 °C 30 s, 72 °C 30 s; followed by final heating at 72 °C 10 min and cooling to 4 °C) using the forward and reverse primers (Table S1 blue). After the PCR product was extracted by Phenol: Chloroform: Isoamyl Alcohol (25:24:1) and precipitated with sodium acetate and ethanol. The DNA pellet was dissolved in ddH_2O and used directly for transcription in vitro.

2.3.2. Preparation of *Nap*-sepharose affinity resin

1 mL of NHS-Activated Sefinose (TM) 4 Fast Flow resin was transferred into a 3 mL empty column and washed with millipore water (ice-cold) and resuspended in 100 mM HEPES buffer (pH 7.4). 0.5 mL **Nap** (12 μM) was added to the resin dropwise under vigorous shaking. The resin was washed with 100 mM HEPES buffer (pH 7.4) and then 100 mM Tris (pH 7.4), following incubation at 25 °C for 4 h. The coupling efficiency was determined by the fluorescence intensity of unreacted **Nap** in the combined wash solutions. Then, the modified resin was sequentially cleaned with filtered deionized water, 100 mM Tris (pH 7.4), and 1 × ASB (20 mM HEPES, 125 mM KCl, 5 mM $MgCl_2$, pH 7.4) repeatedly. The control resin for the negative selection was prepared similarly.

2.3.3. Selection process

For the initial selection round, purified PCR products were transcribed in the reaction solution (4 mL) including 2 mM dN(U)TP, 1 U/μL RNase Inhibitor, and 0.6 U/μL T7 RNA polymerase. After incubation at 37 °C for 2 h, DNase I (50 U/mL) was added and incubated for 30 min. The transcription products were extracted by the mixture solution with Phenol: Chloroform: Isoamyl Alcohol (25:24:1, pH 5) and precipitated in the solution including sodium acetate and ethanol. The RNA pellet was dissolved in 1 × AB buffer (20 mM PBS, 125 mM KCl, 5 mM $MgCl_2$, pH 7.4) and used directly for aptamers screening. Prior to the binding procedure, the RNA was folded by gradient annealing from 75 °C to 25 °C and incubated for an additional 2 h at 25 °C. RNA was first incubated with the mock resin for 2 h at 25 °C for removing nonspecific binding RNA aptamers of resin. The remaining unbound RNA was incubated with the Nap-modified resin under the same conditions. The resin was washed with 1 × ASB buffer over three times and then incubated with 5 mM EDTA at 60 °C for 10 min to elute combined RNAs. The eluted RNA was precipitated by EtOH (added glycogen) and the pellet was dissolved in 100 μL ddH_2O. After the reverse transcription procedure, cDNAs were amplified by PCR procedure, transcribed, and folded identically. The RNA was subjected to the next screening round. The screening was carried out for six rounds using this protocol. From the seventh round, the concentration of **Nap** decreased halve to increase selection pressure, meanwhile, the RNA decreased from 100 μM (rounds 1–2) over 50 μM (rounds 3–6) to 10 μM (rounds 7–12), and then elution RNAs were collected, purified and dissolved in 1 × AB buffer. The screening progress was monitored by the percentage of eluted RNA.

2.3.4. Sanger sequencing

The RNA eluted from 12 rounds of selection was reverse transcribed, PCR amplified and then cloned into a mammalian vector (Tomm20-mApple, Addgene#54955) using a restriction enzyme. The fluorescent protein mApple was replaced with the aptamer sequences through two cleavage sites (*Bam*HI, *Not*I), and the sequence determination from the 5′ to 3′ end was completed through the CMV promoter. The constructed plasmid was transformed into receptive DH5α Escherichia coli (*E. coli*), and 96 colonies were picked from LB culture plates (kanamycin) for Sanger Sequencing. The 48 samples of them with the correct bands were sequenced (Table S2).

2.4. Measurement of the dissociation constant

The dissociation constant (K_d) of the selected aptamers (**NapRA**, Apt-80, Apt-10) in the complex was calculated by fluorescence spectra. The RNA was folded as previously reported and incubated with **Nap** (50 nM). Constant **Nap** was subjected to a fluorescence readout with aptamers concentrations ranging from 0 to 10 mM at 25 °C. The wavelengths of the excitation and emission were 450 nm and 550 nm, and the slit widths were tuned at + 20 nm and − 10 nm, respectively. The Hill equation was used to fit the displayed curve, and the K_d value was measured and calculated using the following equation [15] on the basis of aptamers concentrations:

$$F = F_0 + \frac{(F\infty - F_0) \times \left\{ (K_d + P_0 + [Apt]) - \sqrt{([Apt] - P_0)^2 + K_d \times (K_d + 2[Apt] + 2P_0)} \right\}}{2P_0}$$

here, F is the fluorescence intensity at any given aptamer concentration, F_0 is the fluorescence intensity of free **Nap** with an initial concentration of P_0, F_∞ is the maximum fluorescence intensity reached when all **Nap** is in complex with the aptamer, [Apt] is the final concentration of added aptamer, and K_d is the equilibrium dissociation constant.

2.5. Cell culture and imaging

We prepared a pET28a-mCherry-NapRA expression vector under the control of the T7 promoter and terminator, where one copy of the **NapRA** aptamer with seven complementary base sequences was introduced into the 3′-untranslated region of the red fluorescent protein mCherry gene by restriction enzyme *Xho*I. All the specific primers and inserted sequences were in Table S3.

The BL21(DE3) competent *E. coli* cells were transformed with

pET28a-mCherry-NapRA plasmid. Single colonies of the bacteria were picked and grown overnight in LB medium (50 μg/mL Kanamycin) at 37 °C. Then, 50 μL bacteria solution was added to 5 mL LB medium and cultured at 37 °C with shaking at 200 rpm. At an OD_{600} of 0.3, 1 mM IPTG was added to initiate transcription for an additional 3 h. And then 1 mL bacterial solution was taken up and centrifuged for 2 mins at 12,000 rpm and the supernatant was removed. 100 μL of 8 % PFA solution was added to the bacteria and incubated at room temperature for 10 min after washing with mixture buffer (LB medium with 2 mM $MgSO_4$, 3 mM $MgCl_2$, and 100 μM $CaCl_2$). 20 μL bacterial solution was added to 280 μL mixture buffer and incubated at 37 °C for 1 h, and then the different concentration of **Nap** (2 μM, 1.5 μM, 1 μM, 500 nM, 250 nM, 50 nM) was added, and maintained at 37 ℃ for 30 mins before imaging. The imaging was performed on Laser Scanning Confocal Microscope (Andor iQ 3.2) with a 100 × oil-immersion objective lens (laser combination: 488 nm; 561 nm). Then, Nikon N-SIM Super-Resolution Microscope System was used to perform the super-resolution cell imaging. The ORCA-Flash 4.0 sCMOS camera (Hamamatsu Photonics K.K.) and 100 ×/NA 1.49 oil immersion TIRF objective lens (CFI HP) were used with the motorized inverted microscope ECLIPSE Ti2-E. For Hoechst 33342: λ_{ex} = 405 nm, λ_{em} = 425–475 nm; For **Nap**: λ_{ex} = 488 nm, λ_{em} = 500–550 nm; For mCherry: λ_{ex} = 561 nm, λ_{em} = 580–650 nm.

2.6. Molecular simulation methods

The 3D structure of aptamer was predicted by the RNAComposer system [30,31]. The interactions between **Nap** and **NapRA** were simulated by molecular docking. After the aptamer was defined as a receptor, the possible binding sites for the probe were searched by the Define Site function of DiscoveryStudio software (DS). Three binding sites were obtained, which were named site 1, site 2, and site 3 according to the size of the cavity. The site size was expanded to approximate the probe molecular volume. The probe was applied forcefield of CHARMm and partial Charge of MMFF94 and docked with three different binding sites using default parameters by CDocker in DS, respectively.

3. Results and discussion

3.1. Aggregation property of *Nap*

The absorption and fluorescence spectra of **Nap** in different solvents were first investigated (Fig. 1a and Fig. S1a). With the increase of solvent polarity, the absorption and emission wavelengths of the probe red-shifted due to the intramolecular charge transfer (ICT) effect. The fluorescence intensity of **Nap** in an aqueous solution was about 6-fold lower than that in DMSO. When surfactants were added to the aqueous solutions of **Nap**, the fluorescence and absorption intensities were gradually enhanced (Fig. 1b–c and Fig. S2). The neutral **Nap** can be lit up by four types of surfactants including anionic SDS, zwitterionic BS-12, cationic DTAC, and nonionic Triton X-100. And the fluorescence increased significantly when the micellar concentration exceeded the critical micelle concentration (CMC), suggesting that the turn-on fluorescence responses of **Nap** were driven by molecular disassembly. The weak blue shift (17–25 nm) in emission after the addition of surfactants was due to the fact that the hydrophobic part of the surfactants created a weakly polar microenvironment [32].

To further verify the aggregation of the probe in an aqueous solution, the quantum yield of the probe at different concentrations was measured. We found that the quantum yields of **Nap** in aqueous solutions decreased with increasing probe concentrations (Fig. 1d). Since the higher the concentration, the easier it is to form aggregates, this result also shows the existence of **Nap** aggregates. The dynamic light scattering (DLS) results showed that the size of 5 μM **Nap** was about 132.2 nm (Fig. 1e). In addition, the fluorescence spectra of **Nap** solution remain basically unchanged with the changes of pH (Fig. 1f). This indicated that

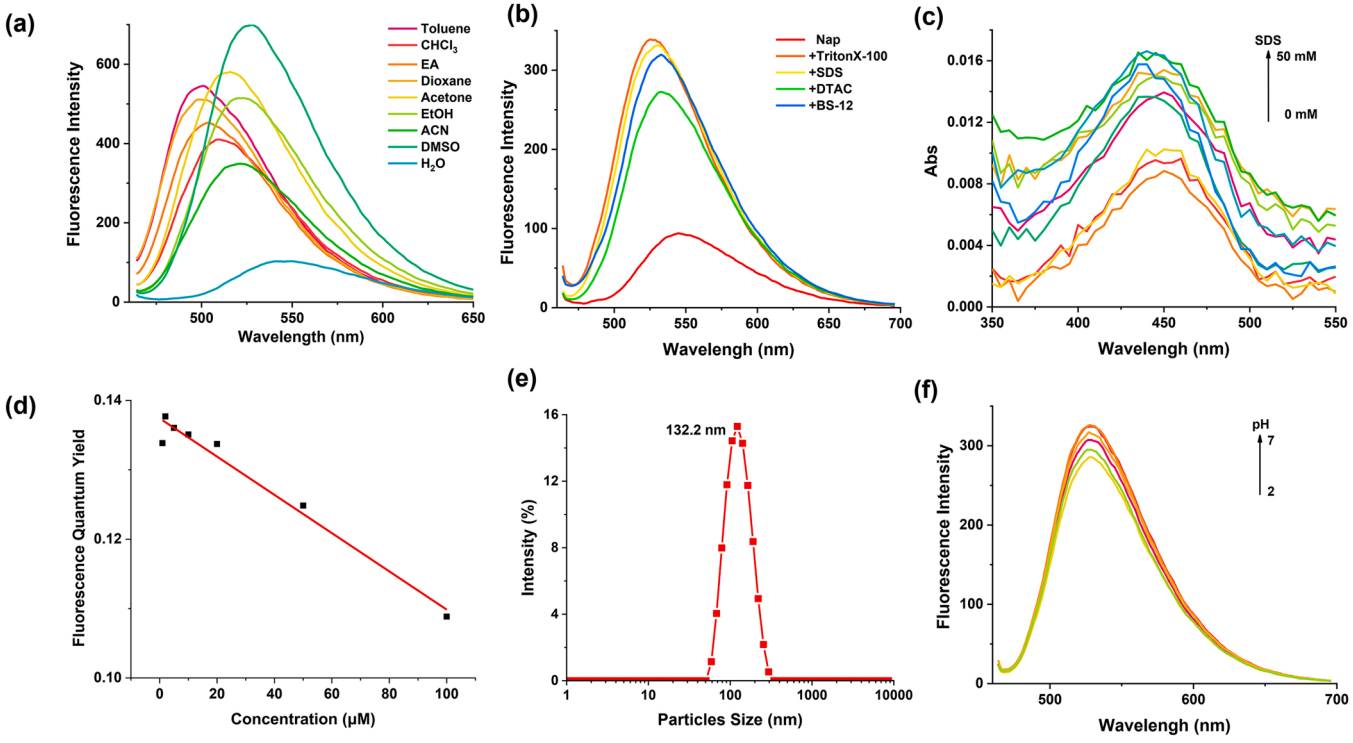

Fig. 1. Aggregation properties of **Nap** in aqueous solution. (a) Fluorescence spectra of 1 μM Nap in various solvents; (b) Fluorescence spectra of 1 μM **Nap** in different types of surfactants; (c) Absorption spectra of 1 μM **Nap** in different concentrations of anionic surfactant SDS; (d) Fluorescence quantum yields of **Nap** at different concentrations in aqueous solution; (e) DLS analysis of 5 μM **Nap** in aqueous solution; (f) Fluorescence spectra of 1 μM **Nap** at different pH with the addition of 50 mM Triton X-100.

there was no photoinduced electron transfer (PET) process, and the disaggregation was the main cause of the fluorescence quenching.

3.2. Selection and identification of a high-affinity aptamer for **Nap**

RNA Aptamers are single-stranded oligonucleotides with a typical length between 25 and 100 nucleotides that fold into three-dimensional structures capable of binding to target molecules. Specific aptamers can be isolated against a large variety of targets through the systematic evolution of ligands by exponential enrichment (SELEX). Here, we used the SELEX technique to screen for specific RNA aptamers of **Nap**. The selection started with an RNA library containing 10^{24} different

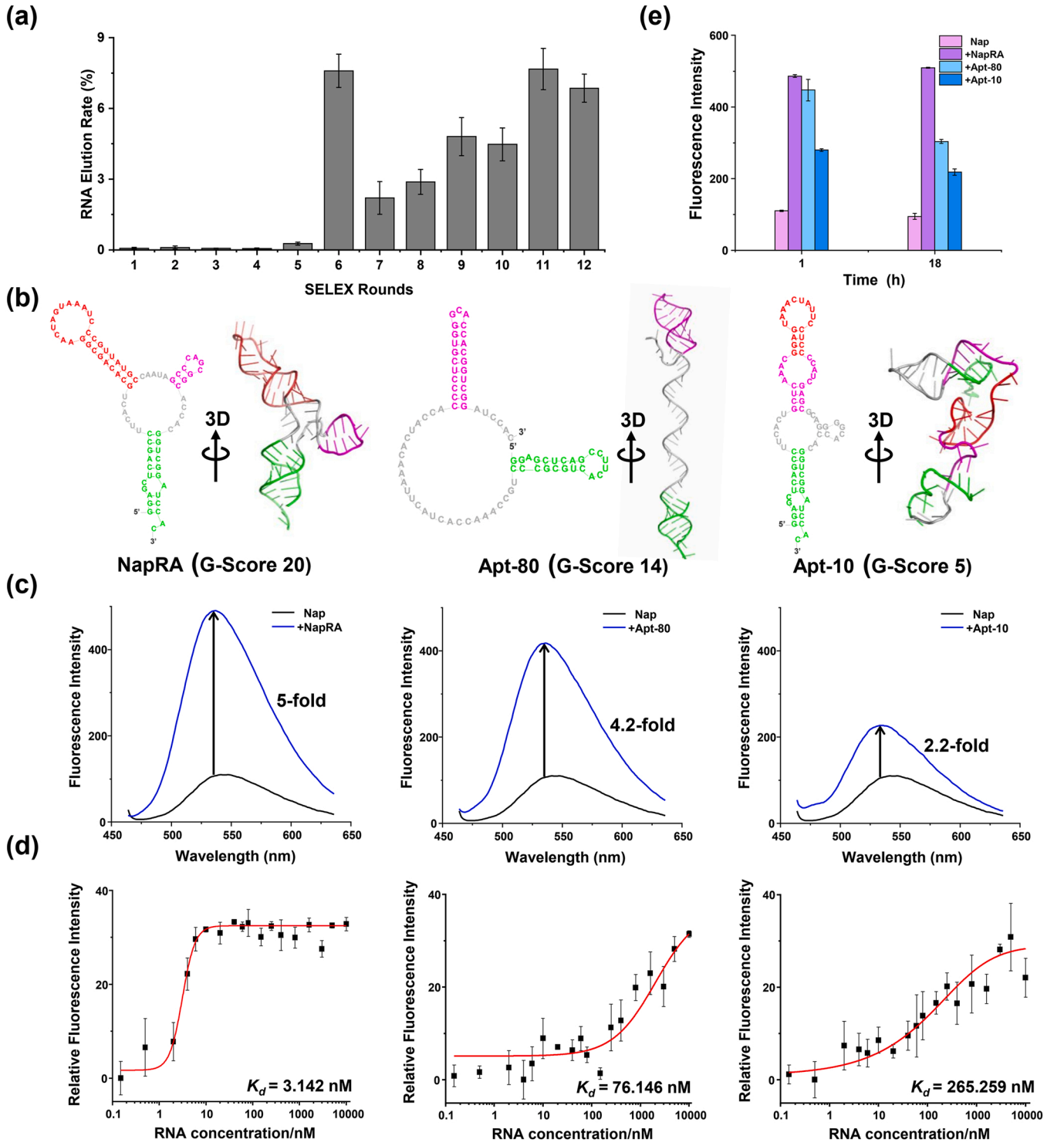

Fig. 2. SELEX screening process and identification of a high-affinity aptamer for **Nap**. (a) Progress of the in vitro selection was monitored by measuring the fraction of RNA eluted from the **Nap**-modified sepharose column. (b) Secondary and tertiary structures of Apt-3 (**NapRA**), Apt-80, and Apt-10 aptamers with corresponding G-score. (c) Fluorescence spectra of 5 μM **Nap** before and after the addition of corresponding aptamers of (b). (d) The affinity of the aptamers to **Nap**, Fluorescence intensities were recorded after incubating **Nap** (50 nM) with different concentrations of the aptamer (0.15 μM to 10 mM). (e) Fluorescence intensity of 5 μM Nap after adding three aptamers and incubating at 37 °C for 1 h and 18 h. Scale bar: 10 μm or 100 nm.

sequences and a standard length of 79-nt. The sequence of the RNA library consisted of a 5′-forward primer binding site, a 40-nt random region, and a 3′-reverse primer binding site. Before the screening, **Nap** was modified onto the NHS-activated sepharose by amidation reaction (Fig. S3). The labeled column showed obvious fluorescence compared to the unlabeled column. The concentration of **Nap** labeled on the sepharose column was approximately 5.739 μM.

A total of 12 rounds of screening were carried out, and the affinity of the remaining RNA to **Nap** increased with the shrinking of the library in each round (Fig. 2b). The in vitro selection was monitored by the percentage of RNA eluted efficiency from the ligand **Nap**. The RNAs were combined with the **Nap**-modified sepharose column and treated to the SELEX following transcription of the first ssDNA library iteratively. Sepharose binding, non-specificity washing, elution of retained RNAs, RNA reverse transcription, and cDNA amplification were all processes in the protocol. RNAs elution rate increased exponentially after 6 rounds of selection, indicating the enrichment of target-binding RNAs. To improve the evolutionary pressure, 7–12 rounds were further performed with dye concentrations that were reduced in half and washing conditions that were progressively tougher. The aptamers with high affinity in the twelfth round were reverse-transcribed, PCR-amplified, and cloned into plasmids that were subsequently transformed into *E. coli*. After PCR of 96 single colonies of bacteria, selected 48 plasmids with target lane (144 bp) were sequenced by Sanger sequencing (Table S2), and 32 plasmids of them were sequenced successfully.

Guanine-rich nucleic acid sequences could fold into a special G-quadruplex (G4) structure which is generally applicable to varieties of dye-based aptamer binding principles sites [14]. Therefore, the obtained aptamers here were further screened through the G-Score evaluation system, which had been used as a standard to predict the RNA G4 structure folding [33]. The G-score of these 32 aptamers sequenced was calculated by QGRS Mapper, which had been gradually used in the field of SELEX in recent years to predict aptamer capability and functional core [34–37]. Finally, nine of them (Apt-3, Apt-10, Apt-44, Apt-51, Apt-52, Apt-66, Apt-74, Apt-80, and Apt-91) were given effective scores from 5 to 20 as shown as Table S4.

Meanwhile, the phylogenetic tree of all 32 aptamers was depicted using the unweighted pair group method with an arithmetic mean (UPGMA) program. The rooted phylogenetic tree revealed the homology of these aptamers' sequences. The higher the sequence homology, the closer the two sequences were to the phylogenetic tree (Fig. S6a); however, this did not imply that their tertiary structures were homologous. For example, Apt-10 with the lowest G-score has a high homology while Apt-3 with the highest G-score (Fig. S6a). The secondary or tertiary structures analyzed by MEGA7 software [38] and the RNA-Composer [39] were shown in Fig. 2c and S5. As the G-score reduced, it showed a gradual decline in the ability to form G4, which would be due to the gradual decrease in the capacity to form interacting units with **Nap**. Therefore, the secondary structure motifs or other domains of these low-score aptamers might influence the interaction with **Nap**. To prove our hypothesis, the sequences corresponding to the ssDNA of the two highest scores (Apt-3, G-Score 20; Apt-80, G-Score 14) and the one with the lowest scores (Apt-10, G-Score 5) were synthesized (Fig. 2b). This three ssDNA was turned into transcripts by the T7 promoter. 12 % denaturing urea PAGE analysis demonstrated that they were successfully transformed into transcripts (lane 1–3 of Fig. S6b) as compared to the control (lane 4 of Fig. S6b), and then they were used after further purification and annealing folding.

The fluorescence changes after **NAP** bound by the screened aptamers were in line with our expectations. After binding to **Nap**, Apt-3 (here and after referred to **NapRA**) with the highest G-Score had the greatest change in **Nap** fluorescence intensity (about 5 times enhancement), while Apt-80 with a relatively low score, enhanced **Nap** fluorescence by about 4.2 times. And Apt-10 with the lowest G-score only increased **Nap** fluorescence by 2 times (Fig. 2c, S6c). It was worth noting that the fluorescence emission wavelength of **Nap** displayed blueshifts (~ 13 nm) after binding to **NapRA**, indicating that the binding cavity in **NapRA** was smaller in polarity than that in the aqueous solution (Table S5). The dissociation constants (K_d) of **Nap** to these three aptamers were measured to be 3.142 nM, 76.146 nM, and 265.259 nM, respectively (Fig. 2d). **NapRA** has the greatest affinity to **Nap**, which coincides with the fact that these two cause the greatest fluorescence enhancement. This K_d value is much higher than that of reported aptamer /dye complexes, such as SiRA-SiR ($K_d = 430 \pm 70$ nM) [28], Corn/DFHO ($K_d = 70$ nM), Squash/DFHBI-1 T ($K_d = 45$ nM) [15], et al. This super binding affinity was the main cause to induce in the disassembly and light-up fluorescence of **Nap**. After incubation at 37 °C for 18 h, The fluorescence of the **Nap**/**NapRA** complex remained stable, while the fluorescence of **Nap** and Apt-80/Apt-10 complex decreased at different degrees. This binding stability is due to the strong binding affinity between **Nap** and **NapRA** (Fig. 2e). Therefore, **NapRA** was selected for further investigation.

3.3. Disaggregation and photostability of *Nap* after binding to *NapRA*

The disaggregation properties of **Nap** induced by aptamer **NapRA** were first characterized by confocal fluorescence imaging. A few fluorescent spots of **Nap** were observed in the aqueous solution, but the fluorescence was weak in general. After the addition of **NapRA**, the fluorescence of the **Nap** aqueous solution was enhanced obviously, and there was no fluorescent spot observed in the imaging (Fig. S7). After evaporation of the aqueous solution, we found that the **Nap** samples showed a large number of rod-like fluorescent aggregates, but these aggregates disappeared after the addition of **NapRA** but were replaced by a few bright fluorescent spots, which should be the aptamer/dye complex. Non-fluorescent aggregates here in the bright field were formed by an excess of aptamers (Fig. 3a). The results of scanning electron microscopy (SEM) were consistent with those of fluorescence imaging. As shown in Fig. 3b, we observed spindle-shaped aggregates with about 100–200 nm wide in aqueous solutions containing **Nap** only, as well as some slender linear structures. The high affinity of **NapRA** to **Nap** induced the disaggregation of **Nap** nanoparticles through competitive binding so that only small-size particles of 10–50 nm were visible in SEM imaging. This disaggregation process was also monitored by DLS, whereas the particle size of **Nap** decreased from 132.2 nm (Fig. 1e) to 65 nm after binding to **NapRA** (Fig. 3c).

In addition to the fluorogenicity and high affinity, the photostability of the probe is the key requirement for successful aptamer-based RNA imaging. **Nap** showed better photo-stability than previously reported photo-stable naphthalimide derivatives via inhibiting twisted intramolecular charge transfer (TICT) (for example 4-azetidine-N-methyl-1,8-naphthalimide) [40], fluorescein and fluorescent proteins mCherry (Fig. 3d). 4-azetidine- 1,8-naphthalimide and mCherry were widely used in SIM imaging for their good photostability [17,41]. More importantly, the photostability of **Nap** after binding to **NapRA** was much higher than **Nap** itself and comparable to Rhodamine 123 which is considered one of the most photostable dyes. Thus, the excellent photostability of **Nap**/-**NapRA** enabled a potential long-term RNA imaging.

3.4. Super-resolution imaging of mRNA in bacteria

Since *E. coli* is an ideal model for RNA imaging [17,28], we fluorescently imaged mCherry mRNA in bacteria with **Nap**/**NapRA** pairs in this work. One copy of the **NapRA** aptamer with seven complementary base sequences was introduced into the 3′-untranslated region of the red fluorescent protein mCherry gene, and the mCherry without **NapRA** as the control group. *E. coli* expressing either mCherry or mCherry-NapRA mRNA were imaged in the presence of **Nap** (Fig. 4). Firstly, bacteria expressing mCherry or mCherry-**NapRA** displayed similar mCherry fluorescence intensities, suggesting that the **NapRA** tag did not affect the transcription and translation processes of the target protein. We then examined the performance of **Nap** in bacteria to selectively bind

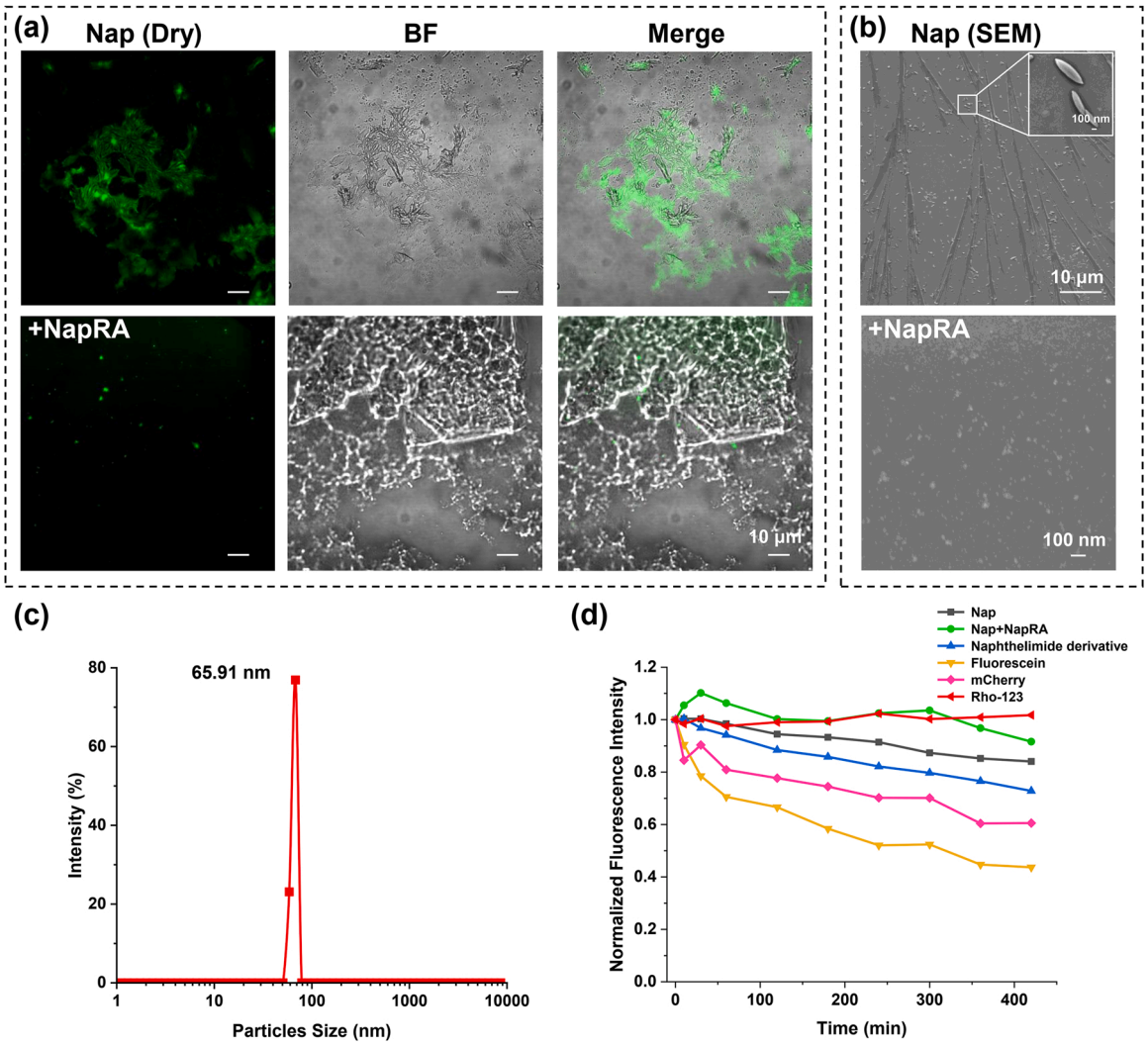

Fig. 3. Disaggregation and photostability properties of **Nap** nanoparticles after the binding of **NapRA** to **Nap**. (a) Confocal imaging of dried samples of 5 μM **Nap** before and after binding to **NapRA**. (b) Scanning electron microscope (SEM) imaging of 5 μM **Nap** before and after binding to **NapRA**. (c) DLS analysis of 5 μM Nap after the addition of 50 μM **NapRA**. (d) Photostability of 5 μM **Nap** in aqueous solution.

NapRA. The bright fluorescence emission of **Nap** was detected predominantly in bacteria expressing mCherry-**NapRA** mRNA, but not in the control cells. As shown in Fig. 4c, there was a 5-fold enhancement of the **Nap** fluorescence inside the mCherry-NapRA-overexpressed bacteria to that in the background, which was consistent with the results of in vitro fluorescence detection (Fig. 2d), indicating the fluorogenic feature of **Nap**/**NapRA** complex. We further incubated bacteria expressing mCherry-NapRA mRNA with different concentrations (50 nM to 2 μM) of **Nap**. We found that the fluorescence intensity in bacteria was 1.5–5 times stronger than that in the background, but the signal-to-noise ratio was the highest when the probe was 1 μM (Fig. S8). This may be due to the lower incubation concentration that would reduce the detected amount of mRNA while increasing **Nap** to 2 μM caused higher background fluorescence.

Structured illumination microscopy has emerged as one of the most universally implemented super-resolution imaging techniques that can surpass the optical diffraction limit [42]. SIM imaging of intracellular proteins, organelle, and cytoskeletal have been well established [41, 43–46], but its applications for RNA imaging are still rare [47,48]. In this work, it proved that the fluorogenicity and photostability of the **Nap**/**NapRA** complex enable **Nap** a useful fluorophore for SIM imaging of mRNA (Fig. 4d-e). The location of mRNA in bacteria was resolved by the colocalization of **NAP** fluorescence with mCherry. Compared with widefield imaging, SIM imaging can clearly distinguish the position of mRNA in bacteria (Fig. 4d). We observed that the fluorescence of mCherry and **Nap** were located in different locations of almost all bacteria, where mCherry was located in the bacterial cytoplasm and most of **Nap** was accumulated in one or two distinct foci of most bacteria.

The general distribution of bacterial mRNAs includes uniform expression throughout the cytoplasm, localization into distinct foci near the nucleoid, formation of helical patterns along the cell axis, and enrichment on the inner membrane, or at the cell poles or the septum during cell division. We further image the bacteria with both **Nap** and Hoechst 33342, which can label the dsDNA of the bacteria. The normalized intensity along the bacteria displayed the fluorescence co-localization imaging between **Nap** and Hoechst 33342 (Fig. 4e–g). It demonstrated that mCherry mRNA localized around the nucleoid of *E. coli*. This result was supported by a previous report [49], where the newly transcribed mRNA first appeared in the nucleoid and then moved to the nucleoid periphery. This was also consistent with our observation that because the bacteria were fixed, the newly generated mRNAs had no time to move to the periphery, and most of them were concentrated in the nucleoid. In addition, Liopis and co-works found that the localization of lacZ mRNA in *E. coli* was accumulated in one or two distinct foci in most fixed cells [50]. Generally, to image RNAs of low abundance and to increase the sensitivity of the system, a large number of tandem

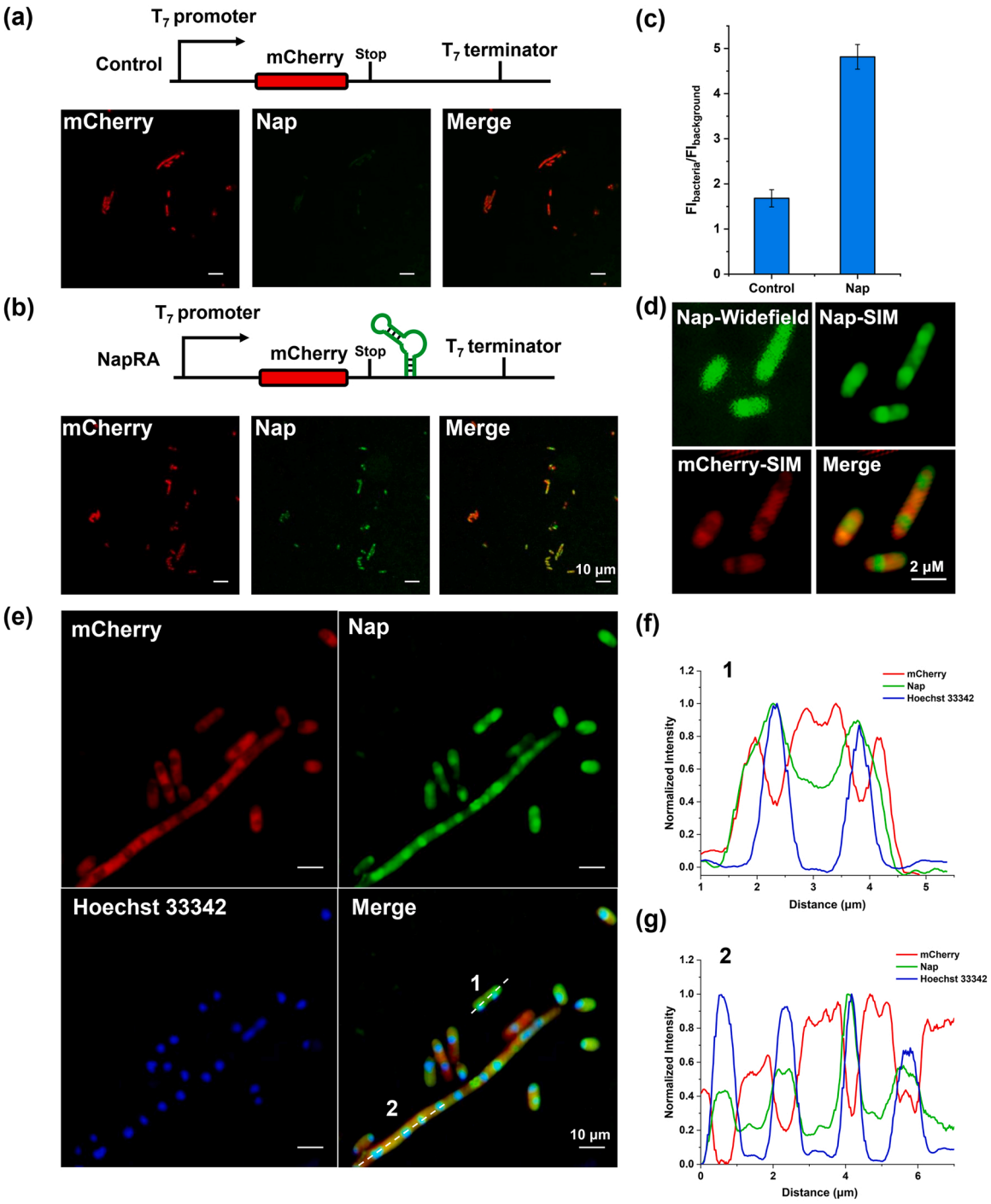

Fig. 4. Confocal and SIM imaging of mRNA in *E. coli*. (a) Expression scheme of mCherry mRNA (control), and no-wash confocal imaging in bacteria with 1 μM **Nap**. (b) Expression scheme of mCherry-**NapRA** mRNA, and no-wash confocal imaging with 1 μM **Nap**. (c) The fluorescence intensity ratio of **Nap** in bacteria to that in the background. (d) Widefield and SIM imaging of *E. coli* expressing mCherry-**NapRA** mRNA treated with 1 μM **Nap**. (e) SIM imaging of *E. coli* expressing mCherry-**NapRA** mRNA treated with 1 μM **Nap** and 500 nM Hoechst 33342. (f) Normalized intensity along the dotted line 1 in (e). (g) Normalized intensity along the dotted line 2 in (e). Scale bar: 10 μm.

repeats RNA aptamers were fused to the RNA of interest. It is worth noting that only one copy of **NapRA** was enough to be used for SIM imaging of bacterial mRNA in this paper and a significant result was obtained.

3.5. *The binding mechanism*

In order to further investigate the binding mechanism between **Nap** and **NapRA**, **Nap** was docked with **NapRA** by DiscoveryStudio (DS) software to explore the possible binding information. Three binding sites were obtained, which were named site 1, site 2, and site 3 according to the size of the cavity (Fig. S9). According to the binding mode, CDocker Energy and the solvent-accessible surface of the probe in the binding cavity, site 1 was the most ideal binding site for **Nap** (Fig. 5a). First, the CDocker Energy score of the probe docked in the site 1 was superior to the other two sites. Second, the solvent-accessible surface of the probe in site 1 didn't cover the chromophore Naphthalimide of the probe molecule, which indicated that the aptamer provided a non-aqueous

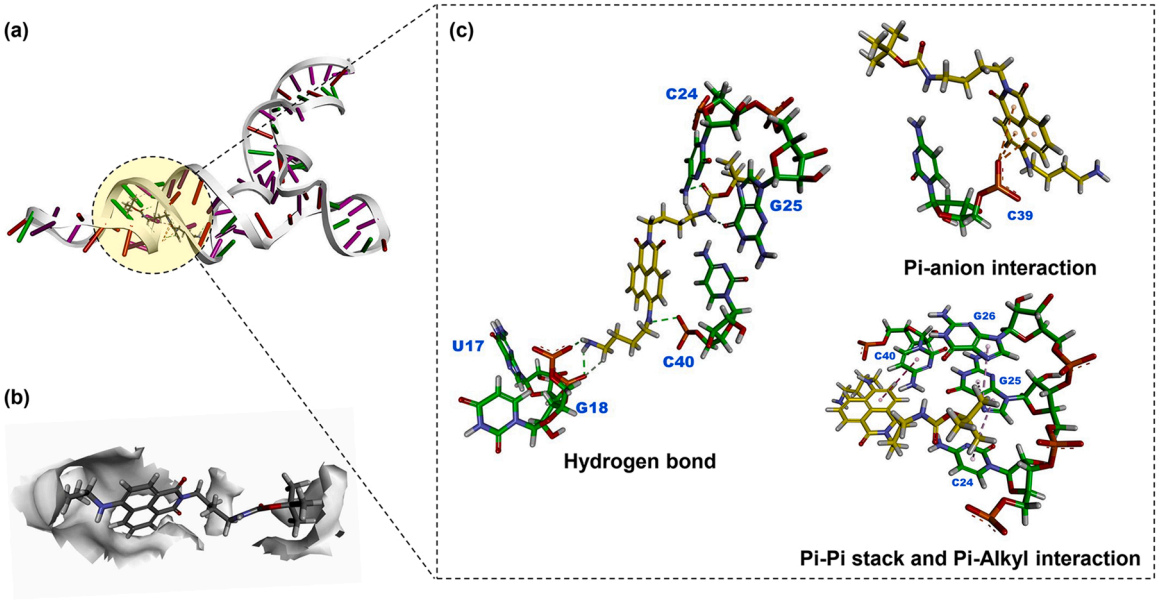

Fig. 5. The docked results of **Nap** and **NapRA**. (a) **Nap** docked in the binding site 1 of **NapRA**; (b) **Nap** in binding site 1 with solvent accessible surface (gray); (c) the interactions between **Nap** (carbon atom in yellow) and **NapRA** (carbon atom in green), green dashed line for hydrogen bond, orange dashed line for Pi-Anion interaction, pink dashed line for hydrophobic interaction.

environment to the probe (Fig. 5b). This is consistent with the fluorescent data of **Nap** in aptamer solution with weak blue shift (~ 13 nm) (Fig. 2d). The tight encapsulation of **Nap** by aptamer **NapRA** isolated **Nap** from reactive oxygen species in water, thus improving its photostability [49,51,52].

Finally, various interactions between **Nap** and binding site 1, including hydrogen bonds, electrostatic interactions, and hydrophobic interactions, ensure the stable binding of the probe to the aptamer. The docked **Nap** molecule was in an extended conformation. There were five pairs of hydrogen bonds (Fig. 5c), including hydrogen bonds between the terminal amine group and the phosphate of U17 and G18, the 4-amine group and the phosphate of C40, the amine group of amide and the carbonyl oxygen of G25, carbonyl oxygen of amide and the amine group of C24. To some extent, the hydrogen bond between the 4-amine group and the phosphate of C40 weakened the electron donor effect of the 4-amine group, which was the main cause of the blue-shifted wavelength of **Nap**. The naphthalimide of the probe and the phosphate of C39 formed a Pi-Anion interaction, which also affected the electron movement of the chromophore "push-pull" system. There were two kinds of hydrophobic interaction, including Pi-Pi stack between the naphthalimide of the probe and the cytosine ring of C40, Pi-Alkyl interaction between the tert-butyl ester chain of the probe and the base aromatic ring of C24, G25, and G26 (Fig. 5c). The hydrophobic interactions were beneficial to stabilization of the complex.

4. Conclusions

In summary, we have developed a dye/aptamer pair **Nap**/**NapRA** for no-wash RNA super-resolution fluorescent imaging. The target RNA aptamer **NapRA** can be lit up by **Nap** with an aggregation-disaggregation effect. The capability of **NapRA** inducing the disaggregation of **Nap** was due to their strong binding affinity of 3.142 nM, which resulted from the synergistic effects of hydrogen bonds, electrostatic interactions, and hydrophobic interactions. Fluorescence imaging, SEM and DLS analysis demonstrated the dispersion of **Nap** nanoparticles from 132 nm to about 65 nm, followed by 5-fold fluorescence enhancement. Significantly, the photostability of **Nap** after binding to **NapRA** was much higher than **Nap** itself in SIM imaging. Finally, we employed the **Nap**/**NapRA** system to visualize the expression of mCherry mRNA in *E. coli* by genetically encoding one copy of **NapRA** to 3′-untranslated regions of mCherry. The SIM imaging showed a strong fluorescence signal mainly appeared near the bacterial nucleoid and around the cytoplasm. It is worth noting that only one copy of NapRA was used and significant SIM imaging result was obtained. We have limited prokaryotic systems in this work, but the application to mammalian cells is currently being studied. We expect that it will be a valuable aptamer system for RNA imaging, and we are enthusiastic about improving this labeling concept for use in eukaryocytes to enable more convenient RNA identification and detection modalities.

CRediT authorship contribution statement

Chunyu Yan: selected the aptamers, measured the spectra, did the cell imaging, and wrote the paper. **Lu Miao:** designed experiments, constructed plasmids, did the cell imaging, and wrote the paper. **Yan Zhang:** measured the spectra. **Xuelian Zhou:** did the imaging. **Guangying Wang:** examined the chemical properties of the dyes. **Yueqing Li:** simulated molecular docking model, and wrote the paper. **Qinglong Qiao:** synthesized the probe and examined optical properties, and wrote the paper. **Zhaochao Xu:** designed experiments, and wrote the paper.

C.Y., Y.Z., X.Z., G.W. and Q.Q. synthesized the probe pair Nap and aptamer NapRA and examined optical properties. C.Y. did the cell imaging. Y.L. did the molecular simulation. C.Y., M.L., Q.Q. and Z.X. wrote the paper.

Declaration of Competing Interest

The authors declare that they have no known competing financial interests or personal relationships that could have appeared to influence the work reported in this paper.

Data Availability

No data was used for the research described in the article.

Acknowledgements

We are grateful for the financial support from the National Natural

Science Foundation of China (22225806, 22078314, 22278394), Dalian Institute of Chemical Physics (DICP I202006, I202142, DICPI202227).

Appendix A. Supporting information

Supplementary data associated with this article can be found in the online version at doi:10.1016/j.snb.2023.133731.

References

[1] P. Le, N. Ahmed, G.W. Yeo, Illuminating RNA biology through imaging, Nat. Cell Biol. 24 (2022) 815–824.
[2] S. Samanta, W. Gong, W. Li, A. Sharma, I. Shim, W. Zhang, et al., Organic fluorescent probes for stochastic optical reconstruction microscopy (STORM): recent highlights and future possibilities, Coord. Chem. Rev. 380 (2019) 17–34.
[3] W. Zhou, X. Fang, Q. Qiao, W. Jiang, Y. Zhang, Z. Xu, Quantitative assessment of rhodamine spectra, Chin. Chem. Lett. 32 (2021) 943–946.
[4] J.G. Bauman, J. Wiegant, P. Borst, P. van Duijn, A new method for fluorescence microscopical localization of specific DNA sequences by in situ hybridization of fluorochromelabelled RNA, Exp. Cell Res. 128 (1980) 485–490.
[5] G. Leone, H. van Schijndel, B. van Gemen, F.R. Kramer, C.D. Schoen, Molecular beacon probes combined with amplification by NASBA enable homogeneous, real-time detection of RNA, Nucleic Acids Res. 26 (1998) 2150–2155.
[6] K. Rombouts, K. Braeckmans, K. Remaut, Fluorescent labeling of plasmid DNA and mRNA: gains and losses of current labeling strategies, Bioconjug. Chem. 27 (2016) 280–297.
[7] E. Bertrand, P. Chartrand, M. Schaefer, S.M. Shenoy, R.H. Singer, R.M. Long, Localization of ASH1 mRNA particles in living yeast, Mol. Cell 2 (1998) 437–445.
[8] J. Biswas, W. Li, R.H. Singer, R.A. Coleman, Imaging organization of RNA processing within the nucleus, CSH Perspect. Biol. 13 (2021) a039453.
[9] A.B. Harbauer, J.T. Hees, S. Wanderoy, I. Segura, W. Gibbs, Y. Cheng, et al., Neuronal mitochondria transport Pink1 mRNA via synaptojanin 2 to support local mitophagy, Neuron 110 (2022) 1516–1531, e1519.
[10] S.Y. Park, H.C. Moon, H.Y. Park, Live-cell imaging of single mRNA dynamics using split superfolder green fluorescent proteins with minimal background, RNA 26 (2020) 101–109.
[11] E. Tutucci, M. Vera, J. Biswas, J. Garcia, R. Parker, R.H. Singer, An improved MS2 system for accurate reporting of the mRNA life cycle, Nat. Methods 15 (2018) 81–89.
[12] R.N. Day, M.W. Davidson, The fluorescent protein palette: tools for cellular imaging, Chem. Soc. Rev. 38 (2009) 2887–2921.
[13] J.S. Paige, K.Y. Wu, S.R. Jaffrey, RNA mimics of green fluorescent protein, Science 333 (2011) 642–646.
[14] R. Micura, C. Hobartner, Fundamental studies of functional nucleic acids: aptamers, riboswitches, ribozymes and DNAzymes, Chem. Soc. Rev. 49 (2020) 7331–7353.
[15] S.K. Dey, G.S. Filonov, A.O. Olarerin-George, B.T. Jackson, L.W.S. Finley, S. R. Jaffrey, Repurposing an adenine riboswitch into a fluorogenic imaging and sensing tag, Nat. Chem. Biol. 18 (2022) 180–190.
[16] K.T. Fam, R. Pelletier, F. Bouhedda, M. Ryckelynck, M. Collot, A.S. Klymchenko, Rational design of self-quenched rhodamine dimers as fluorogenic aptamer probes for live-cell RNA imaging, Anal. Chem. 94 (2022) 6657–6664.
[17] G.S. Filonov, J.D. Moon, N. Svensen, S.R. Jaffrey, Broccoli: rapid selection of an RNA mimic of green fluorescent protein by fluorescence-based selection and directed evolution, J. Am. Chem. Soc. 136 (2014) 16299–16308.
[18] W. Song, G.S. Filonov, H. Kim, M. Hirsch, X. Li, J.D. Moon, S.R. Jaffrey, Imaging RNA polymerase III transcription using a photostable RNA-fluorophore complex, Nat. Chem. Biol. 13 (2017) 1187–1194.
[19] A.D. Ellington, J.W. Szostak, In vitro selection of RNA molecules that bind specific ligands, Nature 346 (1990) 818–822.
[20] C. Tuerk, L. Gold, Systematic evolution of ligands by exponential enrichment: RNA ligands to bacteriophage T4 DNA polymerase, Science 249 (1990) 505–510.
[21] J.R. Babendure, S.R. Adams, R.Y. Tsien, Aptamers switch on fluorescence of triphenylmethane dyes, J. Am. Chem. Soc. 125 (2003) 14716–14717.
[22] X. Chen, D. Zhang, N. Su, B. Bao, X. Xie, F. Zuo, et al., Visualizing RNA dynamics in live cells with bright and stable fluorescent RNAs, Nat. Biotechnol. 37 (2019) 1287–1293.
[23] A. Murata, S. Sato, Y. Kawazoe, M. Uesugi, Small-molecule fluorescent probes for specific RNA targets, Chem. Commun. 47 (2011) 4712–4714.
[24] B.A. Sparano, K. Koide, A strategy for the development of small-molecule-based sensors that strongly fluoresce when bound to a specific RNA, J. Am. Chem. Soc. 127 (2005) 14954–14955.
[25] M. Sunbul, A. Jaschke, SRB-2: a promiscuous rainbow aptamer for live-cell RNA imaging, Nucleic Acids Res. 46 (2018), e110.
[26] M. Sunbul, A. Jäschke, Contact-mediated quenching for RNA imaging in bacteria with a fluorophore-binding aptamer, Angew. Chem. Int. Ed. 52 (2013) 13401–13404.
[27] F. Bouhedda, K.T. Fam, M. Collot, A. Autour, S. Marzi, A. Klymchenko, et al., A dimerization-based fluorogenic dye-aptamer module for RNA imaging in live cells, Nat. Chem. Biol. 16 (2020) 69–76.
[28] R. Wirth, P. Gao, G.U. Nienhaus, M. Sunbul, A. Jaschke, SiRA: a silicon rhodamine-binding aptamer for live-cell super-resolution RNA imaging, J. Am. Chem. Soc. 141 (2019) 7562–7571.
[29] M. Sunbul, J. Lackner, A. Martin, D. Englert, B. Hacene, F. Grun, et al., Super-resolution RNA imaging using a rhodamine-binding aptamer with fast exchange kinetics, Nat. Biotechnol. 39 (2021) 686–690.
[30] M. Antczak, M. Popenda, T. Zok, J. Sarzynska, T. Ratajczak, K. Tomczyk, et al., New functionality of RNAComposer: an application to shape the axis of miR160 precursor structure, Acta Biochim. Pol. 63 (2016) 737–744.
[31] M. Heiat, A. Najafi, R. Ranjbar, A.M. Latifi, M.J. Rasaee, Computational approach to analyze isolated ssDNA aptamers against angiotensin II, J. Biotechnol. 230 (2016) 34–39.
[32] F. Deng, S. Long, Q. Qiao, Z. Xu, The environmental-sensitivity of a fluorescent ZTRS-Cd(ii) complex was applied to discriminate different types of surfactants and determine their CMC values, Chem. Commun. 54 (2018) 6157–6160.
[33] J.D. Beaudoin, R. Jodoin, J.P. Perreault, New scoring system to identify RNA G-quadruplex folding, Nucleic Acids Res. 42 (2013) 1209–1223.
[34] H. Guo, B. Deng, L. Zhao, Y. Gao, X. Zhang, C. Yang, et al., Programmed aptamer screening, characterization, and rapid detection for alpha-conotoxin MI, Toxins 14 (2022) 706.
[35] S. Malhotra, A.K. Pandey, Y.S. Rajput, R. Sharma, Selection of aptamers for aflatoxin M1 and their characterization, J. Mol. Recognit. 27 (2014) 493–500.
[36] M. Moghadam, M. Sankian, K. Abnous, A. Varasteh, S.M. Taghdisi, M. Mahmoudi, et al., Cell-SELEX-based selection and characterization of a G-quadruplex DNA aptamer against mouse dendritic cells, Int. Immunopharmacol. 36 (2016) 324–332.
[37] M. Song, G. Li, Q. Zhang, J. Liu, Q. Huang, De novo post-SELEX optimization of a G-quadruplex DNA aptamer binding to marine toxin gonyautoxin 1/4, Comput. Struct. Biotechnol. 18 (2020) 3425–3433.
[38] M. Khedri, K. Abnous, H. Rafatpanah, M.S. Nabavinia, S.M. Taghdisi, M. Ramezani, Development and evaluation of novel aptamers specific for human PD1 using hybrid systematic evolution of ligands by exponential enrichment approach, Immunol. Invest. 49 (2020) 535–554.
[39] X. Liu, Q. Qiao, W. Tian, W. Liu, J. Chen, M.J. Lang, et al., Aziridinyl fluorophores demonstrate bright fluorescence and superior photostability by effectively inhibiting twisted intramolecular charge transfer, J. Am. Chem. Soc. 138 (2016) 6960–6963.
[40] W. Liu, Q. Qiao, J. Zheng, J. Chen, W. Zhou, N. Xu, et al., An assembly-regulated SNAP-tag fluorogenic probe for long-term super-resolution imaging of mitochondrial dynamics, Biosens. Bioelectron. 176 (2021), 112886.
[41] R. Heintzmann, T. Huser, Super-resolution structured illumination microscopy, Chem. Rev. 117 (2017) 13890–13908.
[42] H. Chen, H. Wang, Y. Wei, M. Hu, B. Dong, H. Fang, et al., Super-resolution imaging reveals the subcellular distribution of dextran at the nanoscale in living cells, Chin. Chem. Lett. 33 (2022) 1865–1869.
[43] W. Liu, J. Chen, Q. Qiao, X. Liu, Z. Xu, A TICS-fluorophore based probe for dual-color GSH imaging, Chin. Chem. Lett. 33 (2022) 4943–4947.
[44] Y. Guo, D. Li, S. Zhang, Y. Yang, J.-J. Liu, X. Wang, et al., Visualizing intracellular organelle and cytoskeletal interactions at nanoscale resolution on millisecond timescales, Cell 175 (2018) 1430–1442, e1417.
[45] J. Chen, W. Liu, X. Fang, Q. Qiao, Z. Xu, BODIPY 493 acts as a bright buffering fluorogenic probe for super-resolution imaging of lipid droplet dynamics, Chin. Chem. Lett. 33 (2022) 5042–5046.
[46] A.D. Cawte, P.J. Unrau, D.S. Rueda, Live cell imaging of single RNA molecules with fluorogenic Mango II arrays, Nat. Commun. 11 (2020) 1283.
[47] X. Chen, D. Zhang, N. Su, B. Bao, X. Xie, F. Zuo, et al., Visualizing RNA dynamics in live cells with bright and stable fluorescent RNAs, Nat. Biotechnol. 37 (2019) 1287–1293.
[48] J.T. Trinh, Q. Shao, J. Guan, L. Zeng, Emerging heterogeneous compartments by viruses in single bacterial cells, Nat. Commun. 11 (2020) 3813.
[49] P. Montero Llopis, A.F. Jackson, O. Sliusarenko, I. Surovtsev, J. Heinritz, T. Emonet, et al., Spatial organization of the flow of genetic information in bacteria, Nature 466 (2010) 77–81.
[50] J.M. Baumes, J.J. Gassensmith, J. Giblin, J.J. Lee, A.G. White, W.J. Culligan, et al., Storable, thermally activated, near-infrared chemiluminescent dyes and dye-stained microparticles for optical imaging, Nat. Chem. 2 (2010) 1025–1030.
[51] L.K. Kumawat, A.A. Abogunrin, M. Kickham, J. Pardeshi, O. Fenelon, M. Schroeder, R.B.P. Elmes, et al., Squaramide—naphthalimide conjugates as "turn-on" fluorescent sensors for bromide through an aggregation-disaggregation approach, Front. Chem. 7 (2019) 354.
[52] M. Wang, Y. Liao, S. Zhang, Q. Yu, J. Huang, G-Quadruplex DNA binding and cytotoxic properties of naphthalimide substituted styryl dyes, Bioorgan. Med. Chem. 28 (2020), 115325.

Chunyu Yan obtained her B.S. degree and M.S. degree from Qingdao University of Science and Technology in 2020. She is currently working toward the Ph.D. degree in analytical chemistry with the Dalian University of Technology. Her research interest is the fluorescent labeling of nucleic acid and aptamer light-up cell imaging.

Lu Miao obtained her Ph.D. degree from Jilin University in 2014. She is currently an associate professor at the Dalian Institute of Chemical Physics, Chinese Academy of Sciences. Her research interest is the development of biomacromolecule (protein and RNA) labeling and the investigation of physiological processes by super-resolution fluorescence imaging.

Yan Zhang obtained her B.S. degree from China University of Geosciences, Wuhan in 2021. She is currently working toward the M.S. degree in analytical chemistry with the Dalian University of Technology. Her research interest is the interprotein of proteins liquid-liquid phase separation by fluorescence imaging.

Xuelian Zhou obtained her B.S. degree from Fuzhou University in 2019. She is currently working toward the Ph.D. degree in analytical chemistry with the Dalian University of Technology. Her research interest is the structure modified of fluorescent protein and expand its application.

Guangying Wang obtained her B.S. degree from Jiangsu Normal University in 2016, and obtained her M.S. degree from Northwest Normal University in 2019. She is currently working toward the Ph.D. degree in analytical chemistry with the Dalian Institute of Chemical Physics, Chinese Academy of Sciences. Her research interest is the structure-fluorescence relationship of pyrene dyes.

Yueqing Li received her PhD in 2006 from Dalian University of Technology under the supervision of Prof. Weijie Zhao. Since then, she works in Dalian University of Technology. Her research is related to the synthesis and modification of natural products with anti-tumor, anti-virus, anti-aging activities. She is interested in QSAR and good at structure-based CADD, especially for illustrating detail interactions between ligand and macromolecules (protein or RNA).

Qinglong Qiao obtained his Ph.D. from Dalian University of Technology in 2018. He is currently an associate professor at the Dalian Institute of Chemical Physics, Chinese Academy of Sciences. His research interest is the development of new fluorophore, fluorescent probe designing and super-resolution fluorescence imaging.

Zhaochao Xu was born in Qingdao, China, in 1979. He received his PhD in 2006 from Dalian University of Technology under the supervision of Prof. Xuhong Qian. Subsequently, he joined Prof. Juyoung Yoon's group at Ewha Womans University as a post-doctoral researcher. Since October 2008, he was a Herchel Smith Research Fellow at University of Cambridge in Prof. David R. Spring's group. In 2011, he moved to Dalian Institute of Chemical Physics, CAS, where he is currently a Professor. His research is focusing on new fluorophore design and structure-fluorescence relationship, protein labeling and sensing, the development of fluorescent probes for the selective recognition and fluorescent imaging of biologically important species, and super-resolution fluorescent imaging.